Magnetic short-range order and magnetic moments of Co-Mn and Ni-Mn alloys

J. W. Cable
Oak Ridge National Laboratory, P.O. Box 2008, Oak Ridge, Tennessee 37831-6393

Y. Tsunoda
Osaka University, Toyonaka, Osaka, 560 Japan
(Received 20 April 1994)

The magnetic behavior of Co-Mn and Ni-Mn alloys is typical of competing interaction systems with regions of ferromagnetism and antiferromagnetism enclosing an intermediate concentration region in which only magnetic short-range order (MSRO) occurs. Neutron diffuse scattering measurements were made on alloys from this intermediate region to characterize the MSRO and to determine the associated magnetic moments. Diffuse peaks indicative of antiferromagnetic short-range order were observed and average sublattice moments were determined by comparison of the integrated diffuse peak intensities with the cross section for Bragg scattering from the alloys with assumed antiferromagnetic long-range order. The average sublattice moment of the Co-Mn alloys is appreciably smaller than that for the Ni-Mn alloys. Recent local density calculations indicate vanishing moments for Ni and Co atoms in fcc antiferromagnets with large wave vectors. If this applies to these alloys, then all of the moment resides at the Mn sites and corresponds to about $1\mu_B$/Mn for the Co-Mn alloys and $4\mu_B$/Mn for Ni-Mn alloys. This moment difference for these otherwise similar systems is attributed to a moment-volume instability of the type more commonly associated with fcc Fe.

INTRODUCTION

The saturation magnetization of CoMn alloys decreases linearly with Mn content and approaches zero at a critical concentration of about 30 at. % Mn.[1] At higher concentrations, there are peaks in the magnetic susceptibility versus temperature data, but the magnitudes of these peaks decrease rapidly with concentration and vanish at about 40 at. % Mn.[2,3] Then, above about 45 at. % Mn, antiferromagnetic long-range order (LRO) is observed.[4] Clearly, these fcc CoMn alloys exhibit a rich diversity of magnetic behavior arising from competing exchange interactions. In the LRO ferromagnetic alloys, large local environment effects occur at the Co sites, and these dramatically reduce the average Co moment with increasing Mn content.[5] The average ferromagnetic moment at the Mn sites is small ($\sim 0.3\mu_B$/Mn), and this is not due to cancellation by antiparallel alignment, since there are no spatially correlated Mn moment fluctuations, such as those observed[6] for ferromagnetic NiMn alloys of the same concentration. The average sublattice moment for the antiferromagnetic alloy Co-48 at. % Mn is also small ($0.6\mu_B$/atom).[4] There are several neutron studies of the magnetic behavior for alloys in the concentration region intermediate between the ferromagnetic and antiferromagnetic regions, but there are contradictory interpretations of the data. Bacon and Cowlam[7] find a (100) diffuse peak for Co-41 at. % Mn that is essentially independent of temperature between 4.2 and 300 K, and because of this thermal behavior, they conclude that this diffuse peak arises mostly from atomic short-range order (ASRO). However, Adachi *et al.*[4] found no (100) diffuse peak at all for Co-36 at. % Mn and conclude that the alloy is disordered completely. More recently, the data of Wildes *et al.*[8] for Co-32 at. % Mn and Co-37 at. % Mn alloys show a (100) diffuse peak with thermal behavior very similar to that reported by Bacon and Cowlam. Wildes *et al.* used polarization analysis to separate the nuclear and magnetic scattering and extracted Cowley ASRO parameters for the first two shells. These show a slight preference for unlike first neighbors and like second neighbors, in agreement with previous determinations[5,7] of the ASRO parameters for these alloys. However, their magnetic cross sections were too small for a meaningful moment determination.

An extensive study of the system was made by Menshikov *et al.*[9] who used magnetization and neutron diffraction techniques to determine the magnetic phase diagram shown in Fig. 1. They find ferromagnetic LRO below 25 at. % Mn and antiferromagnetic LRO above 43 at. % Mn with "superparamagnetism" and "superantiferromagnetism" in the intermediate region. We will use the terms "ferromagnetic SRO" and "antiferromagnetic SRO" interchangeably with this terminology of Menshikov *et al.* Their neutron data at the (110) position show clearly both the development of antiferromagnetic SRO above 36 at. % Mn and the transformation to antiferromagnetic LRO at 43 at. % Mn. However, absolute cross sections were not measured so that moment values were not determined. All of these previous neutron studies for CoMn alloys were made on polycrystalline samples for which the nuclear and magnetic cross sections are small and difficult to measure. In this paper, we report single-crystal neutron measurements designed to examine the magnetic SRO for CoMn alloys in the concentration region intermediate between ferromagnetic and antiferromagnetic LRO. Results for NiMn alloys with the same intermediate magnetic behavior are also presented and

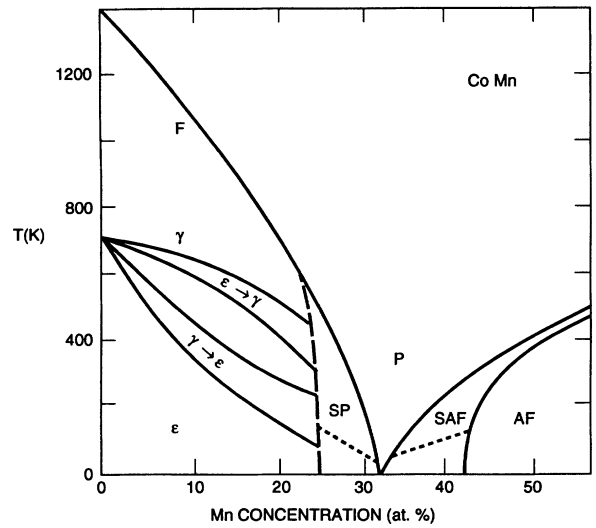

FIG. 1. The magnetic phase diagram for CoMn alloys taken from Ref. 9. The phase regions are P=paramagnetic, F=ferromagnetic, AF=antiferromagnetic, SP=superparamagnetic, and SAF=superantiferromagnetic. The dashed lines indicate blocking temperatures for clusters. γ and ε refer to fcc and hcp crystal structures with a γ-ε martensitic phase transition that vanishes along with ferromagnetism at 25 at. % Mn.

sublattice moments for the two alloy systems are determined and compared. This comparison reveals an average sublattice moment for the NiMn alloys that is appreciably larger than that for CoMn.

EXPERIMENTAL

CoMn alloys

Single-crystal samples of CoMn alloys with nominal concentrations of 25, 30, 35, and 40 at. % Mn were grown by the Bridgman method, annealed at 850 °C for 20 h, and then quenched to room temperature. These compositions span the intermediate region, where magnetic SRO effects should be observable; the 25 and 30 at. % Mn alloys lie within the ferromagnetic SRO region, while the 35 and 40 at. % Mn alloys fall in the antiferromagnetic SRO region. The neutron data were taken using the HB-1 triple-axis spectrometer at the High-Flux Isotope Reactor at the Oak Ridge National Laboratory. Most of the data were taken with the spectrometer set for elastic scattering with an incident energy of 13.7 meV (2.44 Å) and with a pyrolytic graphite monochromator, analyzer, and filter. To gain intensity, some of the preliminary data were taken in two-axis geometry (total scattering) with incident energies of either 14.8 meV (2.35 Å) or 35 meV (1.53 Å).

Some of the 35-meV data are shown in Fig. 2, which gives intensity contours around the (200) fundamental Bragg reflection for the two alloys with ferromagnetic SRO. The most striking feature for Co-25 at. % Mn is the presence of pronounced peaks inside of the (200) at (1.85, ±0.15,0). These peaks have the d spacing of the

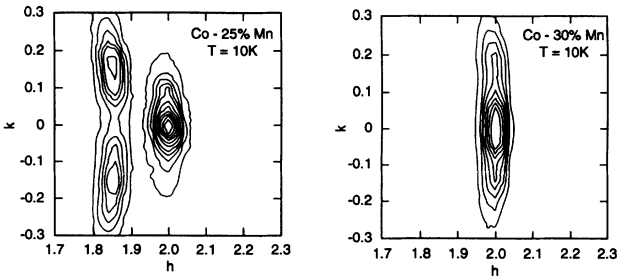

FIG. 2. Intensity contours around (200) for Co-25 and Co-30 at. % Mn at T=10 K. The contour levels range from 50–300 counts/sec.

(101) reflection for the hcp structure indicating that this simple has undergone a martensitic fcc-to-hcp phase transition. According to the phase diagram in Fig. 1, Co-25 at. % Mn develops superparamagnetic clusters below about 500 K and then undergoes a gradual blocking, or freezing, of these clusters below about 150 K. These ferromagnetic SRO clusters should produce diffuse peaks around the fundamental reciprocal lattice points with widths related to the size of the clusters and with intensities proportional to the cluster moment. The presence of such clusters is confirmed here from the full width at half maximum (FWHM) of the observed fcc (200) and hcp (101) peaks. Both sets of peaks are broadened in the transverse direction by mosaic spread, but broadening also occurs in the longitudinal direction where the FWHM is 0.047 reciprocal lattice units (rlu=$2\pi/a_0$) compared with the instrumental resolution of 0.025 rlu. The insets of Fig. 3 show transverse scans fitted to Lorentzian peaks on a background linear in Q. Similar data were taken in 25-K steps over the region from 25 to 300 K, and the variation with temperature of these intensity data is given in Fig. 3. Here, the integrated intensities are approximated by WI_0, where W and I_0 are the fitted peak width and peak height parameters, and the curve labeled (1.85,0,0) represents the sum of WI_0 for both (1.85,±0.15,0) peaks. The intensity decrease for both sets of fundamental peaks shows that part of this scattering is associated with ferromagnetic SRO, and that this occurs in both the fcc and hcp phases. Both phases exhibit a continuous decrease with no anomalous behavior at the blocking temperature of 150 K. Additional furnace data were taken at temperatures up to 600 K, but difficulties were encountered because the hcp phase begins transforming back to the fcc phase above 500 K. There are large hysteresis effects associated with this transition, and the phase composition is not reproducible on thermal cycling through this region. Because of this, we were unable to obtain intensity versus temperature data into the paramagnetic region and therefore could not separate the ferromagnetic SRO scattering from the nuclear Bragg scattering. As a result, the cluster moments for both phases remain undetermined.

The (200) contours for Co-30 at. % Mn are shown in the right panel of Fig. 2. This alloy is above the concentration region for the martensitic phase transition but

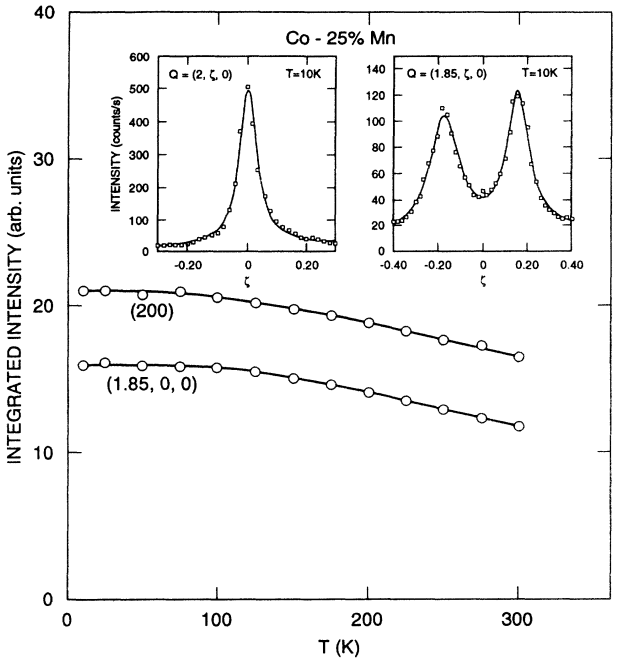

FIG. 3. Temperature dependence of the (200) and the (1.85±0.15,0) intensities for Co-25 at. % Mn. The transverse scans in the inset figures are fitted by the solid curves using Lorentzian peaks and a background linear in ζ. Integrated intensities are approximated by WI_0 where W is the FWHM and I_0 is the peak height.

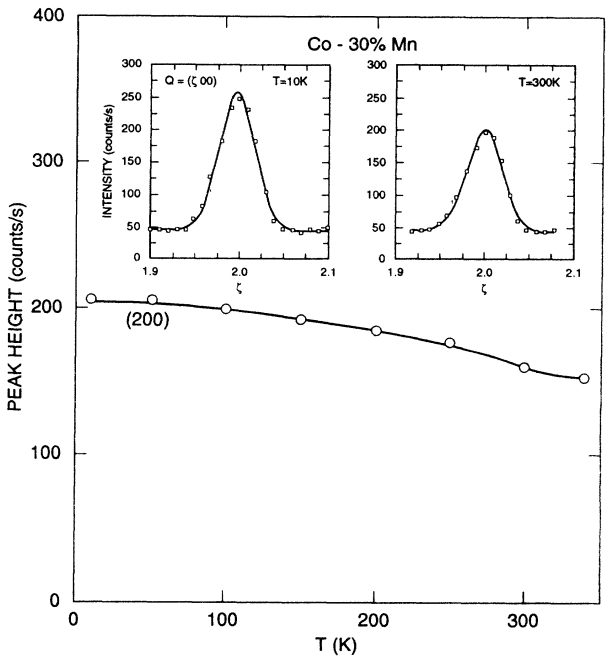

FIG. 4. Temperature dependence of the (200) intensity for Co-30 at. % Mn. The insets show longitudinal scans at $T=10$ and 300 K with solid curves fitted to Gaussian peaks and a linear background. Peak widths are independent of temperature in this range.

still lies in the region for superparamagnetism. The observed peak is very broad in the transverse direction and actually contains at least three peaks due to a bad mosaic distribution. Even so, the temperature dependence of this peak was examined using the narrower longitudinal scans as shown in the inset figures of Fig. 4. These peak widths are also broader than the instrumental resolution and are independent of temperature. The peak height shows a decrease with temperature that is quite similar to that observed for the 25 at. % Mn alloy indicating that at least part of this intensity can be attributed to ferromagnetic SRO. The temperature decrease appears continuous with no indication of either the blocking temperature at 50 K or the transition to the paramagnetic phase at 200 K (see Fig. 1).

Measurements were also made around the superlattice positions for both of these superparamagnetic alloys. The 25 at. % Mn alloy showed no diffuse scattering at these positions, but for Co-30 at. % Mn, diffuse peaks were observed around (100) and (110). Intensity contours for the (100) peak are shown in the left panel of Fig. 6, and temperature dependent data are given in Fig. 5. The elastic scattering data in Fig. 5 are expressed in absolute cross sections obtained by means of an internal calibration using a separately determined background of 2.5 counts/min and the known incoherent (0.305 b/sr/atom) and nuclear disorder (0.089 b/sr/atom) cross sections. The inset figures show (100) longitudinal scans fitted to Lorentzian peaks on a linear background, while the main curves give the temperature variation of the fitted parameters. The peak height decreases with temperature out to about 180 K and then levels off at about 0.060 b/sr/atom. The peak width remains constant at about 0.20 rlu out to 150 K and then becomes less well determined but again constant at about 0.29 rlu in the 200–300 K range. This behavior indicates the presence of both ASRO and anti-

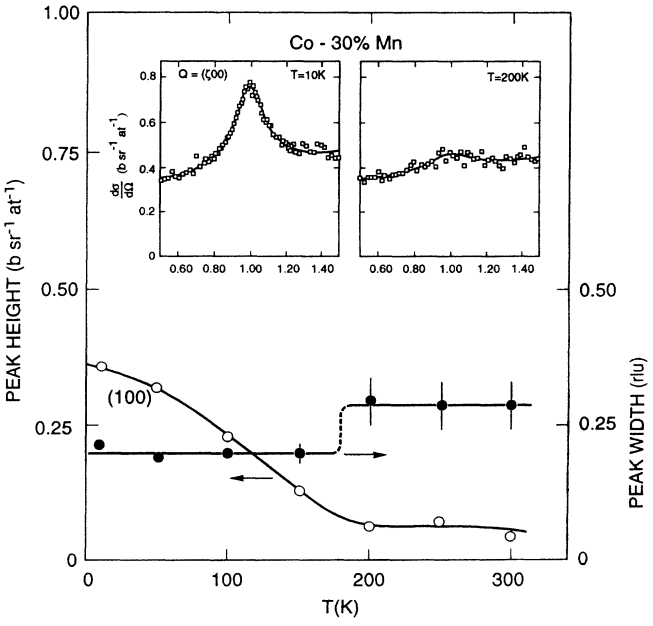

FIG. 5. Longitudinal (100) scans and the temperature dependence of the fitted peak parameters for Co-30 at. % Mn.

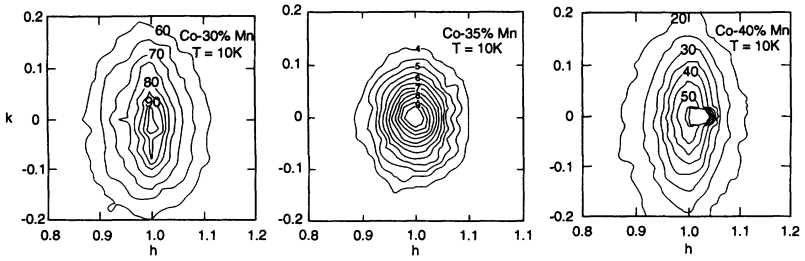

FIG. 6. Intensity contours at (100) for CoMn alloys at $T=10$ K. These are total scattering data with incident energies 14.8 meV for Co-35 at. % Mn and 35 meV for Co-30 and Co-40 at. % Mn. The indicated contour levels are in units of counts/sec.

ferromagnetic SRO below 180 K and only ASRO above that temperature. The observation of diffuse peaks at both the fundamental and superlattice positions for this Co-30 at. % Mn alloy indicates the coexistence of ferromagnetic and antiferromagnetic SRO.

The 35 and 40 at. % Mn alloys both lie in the concentration region for antiferromagnetic SRO, and they exhibit similar neutron-scattering effects. The (100) intensity contours for both alloys are shown in the panels on the right of Fig. 6. The Co-35 at. % Mn sample has a narrow mosaic spread, and as a result, the contours are nearly circular. By contrast, the contours for Co-40 at. % Mn are considerably broader in the transverse direction, and this can probably be attributed to a broad mosaic spread. However, this was not verified because this particular sample is a null matrix alloy with vanishing fundamental Bragg peaks. [The crystal-axis alignment for this sample was accomplished by using the diffuse superlattice peaks, and this was possible only at low temperature where the antiferromagnetic SRO scattering is most intense.] The temperature variation of the (100) peak height and peak width for both compositions are given in Figs. 7 and 8. These elastic scattering data were converted to absolute cross sections by means of the same type of internal calibration as that used for Co-30 at. % Mn. For each alloy, the peak intensity decreases continuously with temperature, and only about 10% of the low-temperature intensity remains at room temperature. This shows clearly that most of the (100) scattering is due to antiferromagnetic SRO. The peaks are very sharp at low temperatures indicating large antiferromagnetic clusters, but the peak widths increase at elevated temperatures as the clusters begin to break apart.

NiMn Alloys

NiMn alloys also exhibit magnetic behavior characteristic of a competing interaction system with ferromagnetic LRO below 24 at. % Mn, antiferromagnetic LRO above 32 at. % Mn, and with spin-glass behavior in the intermediate region.[10,11] Our Bridgman grown Ni-24 at. % Mn and Ni-28 at. % Mn single crystals were annealed at 1000 °C for 24 h and then quenched to room temperature in an attempt to retain as much disorder as possible. Even so, neutron depolarization and critical scattering measurements indicated that our 24 at. % Mn sample has a T_c (240 K), which is appreciably higher than the $T_c=105$ K determined[10] from magnetization measurements on a sample of the same composition. Since the ferromagnetic tendencies of these alloys increase with the degree of ASRO, this suggests that our sample has more ASRO, and this probably results from a slower quench rate due to larger sample dimensions. The (100) intensity contours for Ni-24 at. % Mn are shown in Fig. 9, and the temperature dependence is given in Fig. 10. Here, the elastic 35-meV data are presented in terms of absolute cross sections, which were obtained by means of a vanadium calibration. The peak width is independent of temperature, but the intensity decreases with temperature indicating that at least part of this (100) scattering is due to antiferromagnetic SRO. Comparison of the present low-temperature cross section of 3.5 b/sr/atom with our previous polarization analysis measurements[12] on this same sample, which gives a non-spin-flip, or ASRO, cross section of 1.3 b/sr/atom at (100), indicates that 63% of the scattering is of magnetic origin. The data given in Fig. 11 for Ni-28 at. % Mn are remarkably similar to those shown in Fig. 8 for Co-40 at. % Mn except that, here, the low-temperature cross section is an order of magnitude larger and more of the intensity

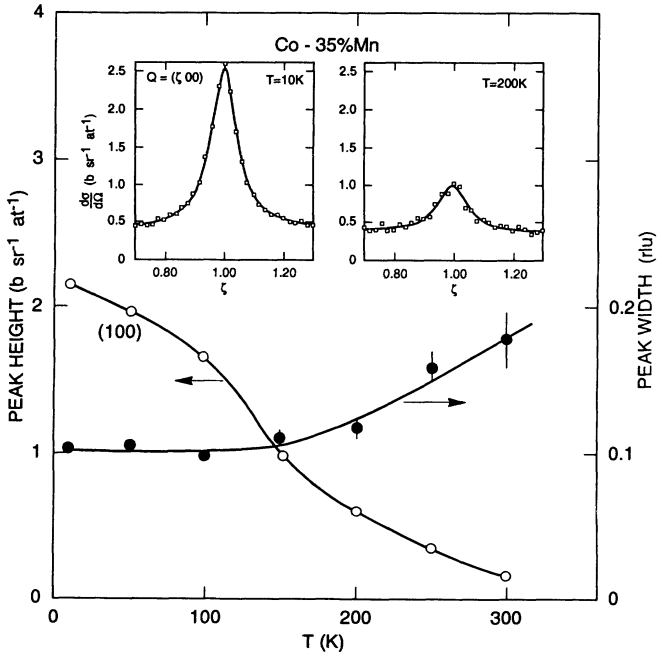

FIG. 7. Longitudinal (100) scans and the temperature dependence of the peak parameters for Co-35 at. % Mn.

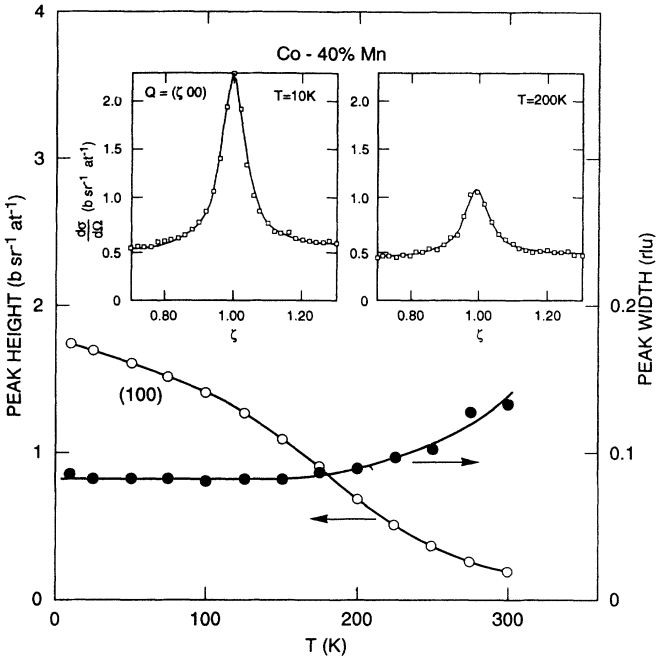

FIG. 8. Longitudinal (100) scans and the temperature dependence of the peak parameters for Co-40 at. % Mn.

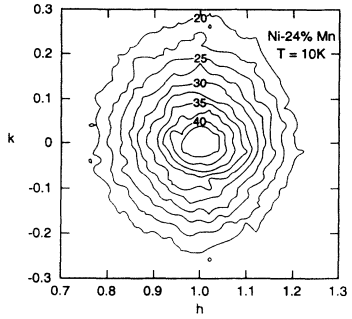

FIG. 9. Intensity contours at (100) for Ni-24 at. % Mn at $T=10$ K. The indicated contour levels are in units of counts/sec. These are 35-meV elastic scattering data.

remains at $T=300$ K. Polarization analysis data are not available for this alloy, but ASRO is undoubtedly present so that part of this (100) scattering should be attributed to nuclear scattering. Nevertheless, the data show massive antiferromagnetic SRO extending over several unit cells.

ANALYSIS

We have performed neutron studies of the magnetic SRO for a series of CoMn and NiMn alloys with concentrations in the region between ferromagnetic and antiferromagnetic LRO. The results show four types of magnetic behavior for this series of alloys: ferromagnetic SRO for Co-25 at. % Mn, coexistent ferromagnetic and antiferromagnetic SRO for Co-30 at. % Mn, coexistent ferromagnetic LRO and antiferromagnetic SRO for Ni-24 at. % Mn, and antiferromagnetic SRO for Co-35 at. % Mn, Co-40 at. % Mn, and Ni-28 at. % Mn. The SRO diffuse peaks have Lorentzian shapes, which implies an ordering that falls off as $(1/R)\exp(-\Gamma R)$, where $\Gamma=W/2$ is the inverse correlation length. The low-temperature parameters are listed in Table I, where Γ_L and Γ_T correspond to the longitudinal and transverse inverse correlation lengths. Parameters for the ferromagnetic SRO diffuse peaks at (200) are not included in Table I because of the complicating factors arising from the martensitic phase transition in Co-25 at. % Mn and from the bad mosaic distribution of Co-30 at. % Mn. This table shows clearly that the peak intensities for the NiMn alloys are an order of magnitude larger than for those CoMn alloys with comparable peak widths. This indication of larger average sublattice moments for NiMn is consistent with previous results.[5,6] for the ferromagnetic alloys, which indicate large Mn moments of about $3.5\mu_B$/Mn for NiMn alloys and small moments of about $0.3\mu_B$/Mn for CoMn alloys.

The average sublattice moment associated with the antiferromagnetic SRO of these alloys was determined from a volume integration of the diffuse peak intensity in Q space and comparison of that integrated cross section with the Bragg scattering cross section from the same alloy with assumed antiferromagnetic LRO. The integrated diffuse peak intensity is given by

$$I=4\pi I_0\Gamma^2\left[q_{\max}-\Gamma\tan^{-1}\frac{q_{\max}}{\Gamma}\right], \quad (1)$$

which is an approximation, since the peaks are actually Lorentzian only at small q, and the integral depends on the integration limit, $q_{\max}$. Nevertheless, reasonable in-

TABLE I. Diffuse-peak parameters and (100) average sublattice moments of CoMn and NiMn alloys.

Sample	I_0(b/sr/atom)	Γ_L (rlu)	Γ_T (rlu)	I	Percent MSRO	$\bar{\mu}$
Co-30 at. % Mn	0.36	0.108	0.137	0.024	83	0.4
Co-35 at. % Mn	2.16	0.052	0.065	0.022	91	0.4
Co-40 at. % Mn	1.74	0.043	0.086	0.023	88	0.4
Ni-24 at. % Mn	2.95	0.157	0.200	0.35	63	1.3
Ni-28 at. % Mn	25.7	0.045	0.049	0.17	95	1.1

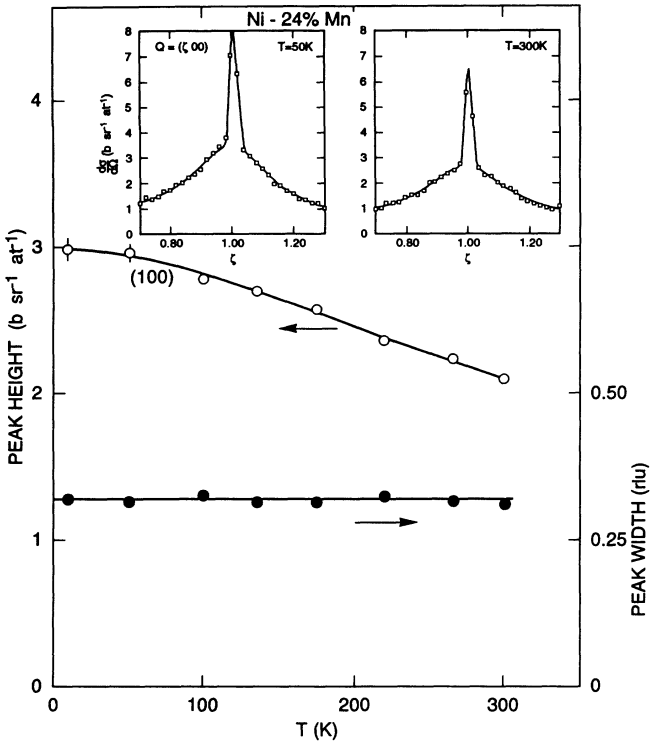

FIG. 10. Longitudinal (100) scans and the temperature dependence of the fitted parameters for Ni-24 at. % Mn. The sharp peaks superimposed on the diffuse peaks in the insets arise from $\lambda/2$ Bragg scattering.

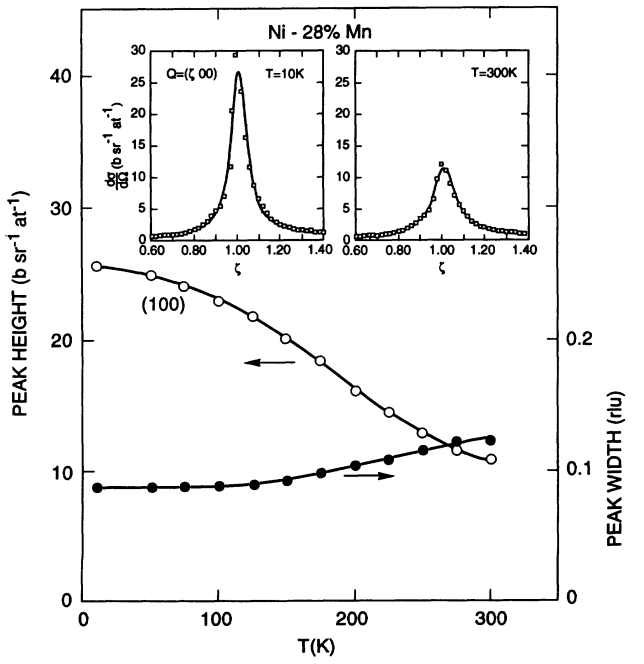

FIG. 11. Longitudinal (100) scans and the temperature dependence of the fitted parameters for Ni-28 at. % Mn.

tegrated intensities are obtained by selecting the smallest q_{max} for which $I(q)=I_0/(\Gamma^2+q^2)$ approaches background. In practice, this requires q_{max} to be about 4 or 5 times the correlation length. The integrated intensities listed in Table I were obtained by assuming spherical volumes with $I(q)$ defined by the average correlation length $\Gamma=(\Gamma_L+2\Gamma_T)/3$ and by integrating to $q_{max}=0.3$ rlu for the three alloys with sharp peaks and to the Brillouin-zone boundary ($q_{max}=0.5$ rlu) for the two alloys with broad peaks. These diffuse-peak intensities must be corrected for their ASRO components before being compared with the cross section for magnetic Bragg scattering. These correction factors are given in Table I under "percent MSRO;" they were taken from the temperature variation of I_0 for the CoMn alloys and calculated assuming that the polarization analysis measurement of the ASRO cross section (1.3b/sr/atom) for Ni-24 at. % Mn also applies to Ni-28 at. % Mn. The corrected diffuse peak intensities can be compared directly with the cross section for magnetic Bragg scattering. For a given Bragg peak at $Q=\tau$, this is given by

$$\frac{d\sigma}{d\Omega}(Q=\tau)=N\frac{(2\pi)^3}{V_0}q^2F(\tau)^2\,, \tag{2}$$

where N is the number of unit cells, $V_0=a_0^3$ is the unit cell volume, q is the magnetic interaction vector, and $F(\tau)$ is the magnetic structure factor per unit cell. For all of these alloys, the (100) and (110) diffuse-peak intensity ratios are the same as the square of the magnetic form factors $f(\tau)$. This indicates the same geometrical structure factors for the antiferromagnetic SRO peaks, and for the present calculation, we assume the full structure factor. Then, with $q^2=2/3$, the cross section per atom becomes

$$\frac{d\sigma}{d\Omega}(Q=\tau)=\left[\frac{2\pi}{a_0}\right]^3\frac{8}{3}p(\tau)^2\,, \tag{3}$$

where $p(\tau)=0.27f(\tau)\bar{\mu}$ is the magnetic scattering amplitude for an atom with the average sublattice moment $\bar{\mu}$. Comparison of Eq. (3) with the corrected diffuse peak intensities gives the $\bar{\mu}$ values listed in Table I. We estimate these average sublattice moments to have an uncertainty of about 20%.

DISCUSSION

As shown in Table I, the average sublattice moments are approximately a factor of 3 smaller for CoMn than for NiMn. If we accept the result of a recent local density calculation[13] that moments of both fcc Co and fcc Ni vanish for antiferromagnetic systems with wave vectors larger than about 0.5 rlu, then these average moments are associated only with the Mn sites and therefore correspond to Mn moments of about $1\mu_B$/Mn for the CoMn alloys and $4\mu_B$/Mn for NiMn. This remarkable difference for the Mn moments in these two, otherwise similar, alloy systems is probably related to a moment-volume instability of the type more commonly associated with fcc Fe.[14] Local-density, spin-polarized band-structure calculations show a similar instability region for

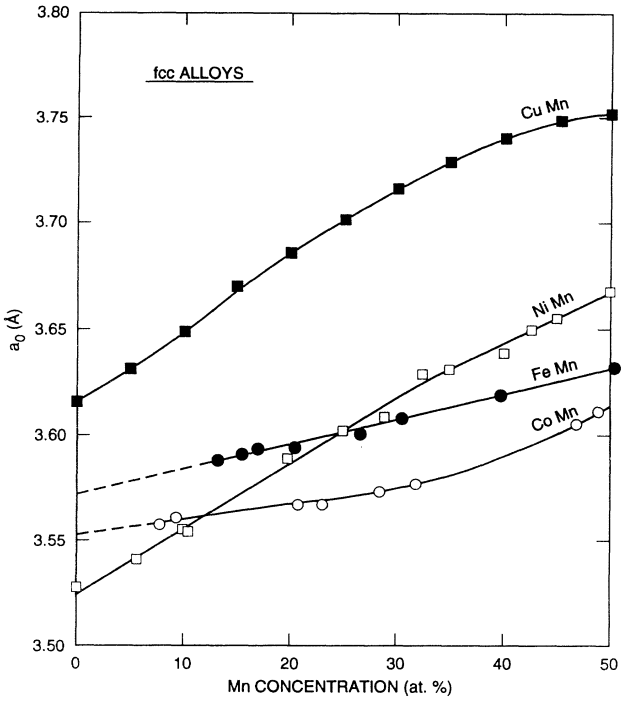

FIG. 12. Lattice constant vs Mn concentration for fcc FeMn, CoMn, NiMn, and CuMn alloys.

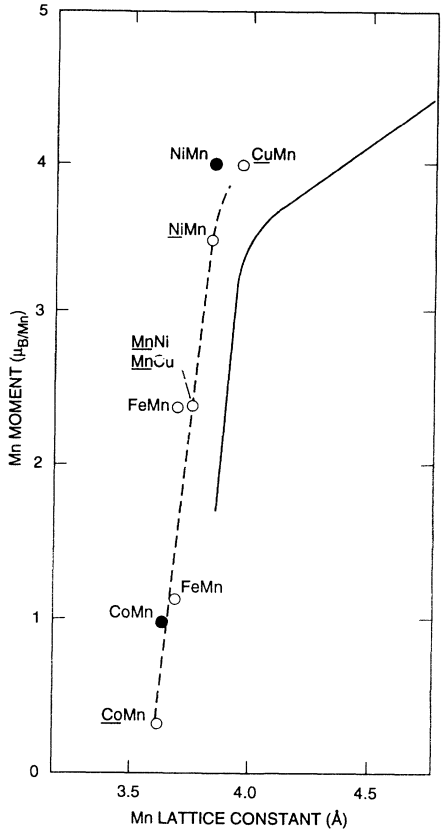

FIG. 13. Magnetic moment of Mn vs the fcc lattice constant. The solid curve is from a ferromagnetic band-structure calculation by Brener *et al.* (Ref. 15), and the filled data points are the present results with effective Mn lattice constants taken from the data in Fig. 12. The open data points represent previous Mn moment determinations and effective Mn lattice constants for *Co*Mn (Ref. 5), FeMn (Refs. 16 and 17), *Mn*Cu (Ref. 20), *Mn*Ni (Ref. 21), *Ni*Mn (Ref. 6), and CuMn (Refs. 18 and 19).

fcc Mn with a discontinuous change from a low-spin state to a high-spin state with increasing lattice constant.[15] The lattice constant data for fcc 3*d*-Mn alloys support this interpretation, since a_0 increases rapidly with Mn concentration for CuMn and NiMn alloys but shows only a small increase for the FeMn and CoMn alloys. Thus, the Mn atoms occupy large volumes and have large moments in the NiMn and CuMn systems but have small volumes and small moments in FeMn and CoMn. As shown in Fig. 12, the curves are sufficiently linear below 40 at. % Mn to suggest the use of Vegard's law to extract the effective Mn atomic size for each of the alloys. This extrapolation yields an effective Mn lattice constant, a_0(Mn), and these are appreciably different for the two alloy subsets: a_0(Mn)=3.69 and 3.63 Å for FeMn and CoMn, and a_0(Mn)=3.83 and 3.94 Å for NiMn and CuMn. This large difference in Mn atom size applies only to the concentration region below about 40 at. % Mn, since none of these lattice constant dependencies follow Vegard's law over the entire concentration region. Indeed, the data at the higher concentrations in Fig. 12 show decreasing slopes for CuMn and NiMn and an increasing slope for CoMn such that the lattice constants for all three alloys converge toward the same value (~3.74 Å) in the Mn-rich region of the phase diagram.

TABLE II. Mn moment versus Mn lattice constant.

Alloy	Magnetic type	μ_B/Mn	a_0(Mn) (Å)	Reference
CuMn	antiferromagnetic SRO	4.0	3.94	18,19
NiMn	antiferromagnetic SRO	4.0	3.83	Present
*Ni*Mn	ferromagnetic	3.5	3.83	6
*Mn*Cu	antiferromagnetic	2.4	3.74	20
*Mn*Ni	antiferromagnetic	2.4	3.74	21
FeMn	antiferromagnetic	1.2,2.4	3.69	16,17
CoMn	antiferromagnetic SRO	1.0	3.63	Present
*Co*Mn	ferromagnetic	0.3	3.63	5

Neutron-scattering methods have been used to determine the magnetic moment at the Mn sites for several fcc alloy systems, and it is interesting to compare the Mn moment versus Mn lattice constant observations with the band-structure calculation by Brener *et al.*[15] Observations are collected in Table II where lattice constants are taken from Vegard's law extrapolations and references are for the Mn moment determinations. Figure 13 gives a comparison of the calculated and observed moment-volume relationship, and there is good qualitative agreement in that both curves show a strong dependence of the Mn moment on the Mn lattice constant. This qualitative agreement is all that can be expected from this comparison because the Mn lattice constants are approximate values based on rather extended linear extrapolations. However, the trend of the observed moment-volume relationship should be valid. Perhaps of more interest is the fact that the observations are for various types of magnetic order ranging from ferromagnetism to antiferromagnetic SRO, while the calculation is for an assumed ferromagnetic state. This seems to indicate that the magnetic moment of a Mn atom depends mainly on the volume available to that atom. As shown in Fig. 13, this moment-volume correlation remains valid even for the intermediate concentration region.

ACKNOWLEDGMENT

This research was supported in part by the Division of Materials Sciences, U.S. Department of Energy, under Contract No. DE-AC05-84OR21400 with Martin Marietta Energy Systems, Inc.

[1]J. S. Kouvel, J. Phys. Chem. Solids **16**, 107 (1960).
[2]M. Matsui, T. Ido, K. Sato, and K. Adachi, J. Phys. Soc. Jpn. **28**, 791 (1970).
[3]D. R. Rhiger, D. Muller, and P. A. Beck, J. Magn. Magn. Mater. **15-18**, 165 (1980).
[4]K. Adachi, K. Sato, M. Matsui, and S. Mitani, J. Phys. Soc. Jpn. **35**, 426 (1973).
[5]J. W. Cable, Phys. Rev. B **25**, 4670 (1982).
[6]J. W. Cable and H. R. Child, Phys. Rev. B **10**, 4607 (1974).
[7]G. E. Bacon and N. Cowlam, J. Phys. C **3**, 675 (1970).
[8]A. R. Wildes, S. J. Kennedy, L. D. Cussen, and T. J. Hicks, J. Phys. Condens. Matter. **4**, 8961 (1992).
[9]A. Z. Menshikov, G. A. Takzei, Yu. A. Dorofeev, V. A. Kazantsev, A. K. Kostyshin, and I. I. Sych, Sov. Phys. JETP **62**, 734 (1985).
[10]W. Abdul-Razzaq and J. S. Kouvel, Phys. Rev. B **35**, 1764 (1987).
[11]O. Moze, T. J. Hicks, and P. von Blanckenhagen, J. Magn. Magn. Mater. **42**, 103 (1984).
[12]J. W. Cable, R. M. Nicklow, and Y. Tsunoda, Phys. Rev. B **36**, 5311 (1987).
[13]L. M. Sandratskii and J. Kubler, J. Phys. Condens. Matter. **4**, 6927 (1992).
[14]V. L. Moruzzi, P. M. Marcus, K. Schwartz, and P. Mohn, Phys. Rev. B **34**, 1784 (1986).
[15]N. E. Brener, G. Fuster, J. Callaway, J. L. Fryand, and Y. Z. Zhao, J. Appl. Phys. **63**, 4057 (1988).
[16]Y. Ishikawa and Y. Endoh, J. Appl. Phys. **39**, 1318 (1968).
[17]S. J. Kennedy and T. J. Hicks, J. Magn. Magn. Mater. **81**, 56 (1989).
[18]P. Wells and J. H. Smith, J. Phys. F **1**, 763 (1971).
[19]J. W. Cable, S. A. Werner, G. P. Felcher, and N. Wakabayashi, Phys. Rev. Lett. **49**, 829 (1982).
[20]N. Cowlam and A. M. Shamah, J. Phys. F **11**, 27 (1981).
[21]O. Moze and T. J. Hicks, J. Phys. F **12**, 1 (1982).